

Stochastic 3D Modeling of $\text{La}_{0.6}\text{Sr}_{0.4}\text{CoO}_{3-\delta}$ Cathodes Based on Structural Segmentation of FIB-SEM Images

Gerd Gaiselmann^{a,*}, Matthias Neumann^a, Lorenz Holzer^{b,c}, Thomas Hocker^b, Michel Prestat^{c,d}, Volker Schmidt^a

^a*Institute of Stochastics, Ulm University, D-89069 Ulm, Germany*

^b*Institute of Computational Physics, ZHAW Winterthur, CH-8400 Winterthur, Switzerland*

^c*Laboratory for High Performance Ceramics, EMPA, CH-8400 Dübendorf, Switzerland*

^d*Nonmetallic Inorganic Materials, ETH Zürich, CH-8093 Zürich, Switzerland*

Abstract

A stochastic microstructure model is developed in order to describe and simulate the 3D geometry of two-phase microstructures (solid and pore phase), where the solid phase consists of spherical particles being completely connected with each other. Such materials appear e.g. in $\text{La}_{0.6}\text{Sr}_{0.4}\text{CoO}_{3-\delta}$ (LSC) cathodes of solid oxide fuel cells, which are produced by screen printing and sintering of a paste consisting of LSC powder manufactured by flame spray synthesis. Thus, as a model type, we consider (fully parameterized) random sphere systems which are based on ideas from stochastic geometry and graph theory. In particular, the midpoints of spheres are modeled by random point processes. In order to assure the complete connectivity of the spheres, a modified version of the relative neighborhood graph is introduced. This graph controls the radii of spheres such that a completely connected sphere system is obtained. The model parameters are exemplarily fitted to three different materials for LSC cathodes, produced with sintering temperatures of 750, 850 and 950°C, respectively. Finally, the goodness of fit is validated by comparing structural characteristics of real and simulated image data.

Keywords: 3D Imaging, Connectivity, FIB-Tomography, Germ-Grain Model, Hough Transform, MIEC Cathode Material, Point Pattern Analysis, Random Geometric Graph, SOFC, Sphere Representation, Watershed Transformation

1. Introduction

In this paper the microstructure of $\text{La}_{0.6}\text{Sr}_{0.4}\text{CoO}_{3-\delta}$ (LSC) cathodes in solid oxide fuel cells (SOFC) is investigated. For classical SOFC electrodes (e.g. Ni-YSZ anodes or LSM-YSZ cathodes) microstructure effects are widely discussed in literature, see [1, 2, 3, 4, 5, 6]. However, modern electrode frequently consists

*Corresponding author: phone: +49 731 50 23590, fax: +49 731 50 23649, e-mail: gerd.gaiselmann@uni-ulm.de

of mixed ionic-electronic conductors (MIEC), such as LSC [7, 8, 9, 10, 11, 12, 13]. The microstructure effects of these MIEC materials on the electrochemical kinetics are not yet well understood. For this purpose quantitative investigations of their microstructures are required.

SOFC operate at high temperatures up to 1000°C, which increase the kinetics of transport processes (e.g. diffusion of oxygen-ions through the solid electrolyte) and of electrochemical reactions (i.e. oxidation of fuel on the anode side and reduction of oxygen on the cathode side). Current research activities are strongly focusing on intermediate temperatures, i.e. 500-600°C, in order to decrease degradation rates and enhance the life-time. When lowering the temperature, transport and reaction kinetics decrease and, consequently, many of the traditional materials used in high temperature SOFC are not suitable for intermediate temperature applications. However, LSC is a material which still provides fast charge transport kinetics and a high efficiency towards oxygen reduction at intermediate temperatures, see e.g. [14, 15, 16, 17].

As a MIEC, LSC provides several parallel reaction pathways, including transport of oxygen through the bulk of the perovskite, through the pores and along the particle surface [18]. In the last decade, most of the attention has been focused on the investigation of the bulk pathway that is seen as dominant for the $La_{0.6}Sr_{0.4}CoO_{3-\delta}$ composition [17]. The bulk pathway comprises the incorporation of oxygen within the crystalline structure of the MIEC (also called "oxygen exchange") followed by oxygen bulk diffusion towards the electrode/electrolyte interface where charge transfer, which is assumed as facile, occurs. The overall kinetics of oxygen reduction as well as the optimized microstructure are therefore controlled by the competition between oxygen exchange and bulk diffusion. When oxygen bulk diffusion is rate-determining, thin dense electrodes are desired. In contrast, if oxygen exchange is a slow reaction step, as often reported for LSC, porous microstructures with large inner surface area are favored to create as many oxygen exchange sites at the electrode/air interface as possible. This can be achieved either by increasing the cathode thickness [11] and/or decreasing the grain size down to the nanoscale [9, 10]. The working hypothesis of the current experimental investigation was to reduce the sinter temperature as far as possible in order to limit grain growth, keep nanoscaled particles and provide high surface area for oxygen exchange. However, when using this strategy, bottlenecks between the LSC grains tend to define narrow constrictions that may question to a large extent the starting assumption of fast bulk diffusion.

In order to study the effect of varying sinter temperatures on the cathode performance it is necessary to analyse the resulting changes of the microstructure which influences oxygen transport (i.e. tortuosity, constrictivity, solid and pore volume fractions) and oxygen reduction kinetics (i.e. surface area). Therefore, in the present paper, we focus on developing a stochastic model which is able to describe and simulate the 3D morphology of LSC cathodes in solid oxide fuel cells produced with varying sinter temperatures.

The motivation for the development of a stochastic microstructure model is related to the methodologies for virtual materials design, which we intend to establish for SOFC electrodes. For the virtual materials design it is crucial to

detect quantitative relationships between the production process (e.g. variation of sinter temperatures and/or change of pore former contents) and the resulting microstructures on a statistical basis. In a further step, microstructure realizations from the stochastic model can be combined with physical simulations, e.g. finite element modeling (FEM), for virtual scenario analyses. Thereby, model-based morphologies of LSC cathodes are transformed into grid representations of the microstructures which are used as a basis for FEM, in order to simulate the effect of microstructure variations on the electrode performance (e.g. ohmic resistance, polarization resistance). In this way, the results of our simulations can be used for microstructure optimization while reducing the amount of expensive experiments in real laboratories. The development of a suitable stochastic model for LSC-cathodes, which is the focus of the present paper, represents an important corner stone in the methodological framework of a future virtual materials design that enables the purposeful optimization of the electrode microstructures.

Our investigations are based on grayscale images gained by high-resolution focused-ion-beam (FIB) tomography, see [19]. In particular, the stochastic microstructure model is fitted to three data sets from FIB-tomography, representing LSC cathodes where the sinter temperature is varied from 750 over 850 to 950°C, see [13]. We denote these three materials according to the considered sinter temperature by LSC-750, LSC-850 and LSC-950, respectively.

Since the LSC microstructure is dominated by a dense packing of spherical particles, our first aim is to represent the LSC phase by a union of moderately overlapping spheres, similar to the structural segmentation procedure proposed in [20] for networks of nanoparticles in organic-inorganic composites. This structural segmentation reduces the number of parameters describing the 3D microstructure of LSC cathodes drastically, since the representation of 3D image data is changed from billions of voxel to thousands of spheres.

The unions of spheres extracted from LSC data can be regarded as realizations of marked point processes in 3D where the midpoints of spheres are the locations of points and the corresponding radii are their marks. The advantage of this off-grid representation is that the microstructure of LSC cathodes represented by unions of spheres can be described by point-process models which form a fundamental class of models in stochastic geometry, see [21, 22]. We thus develop a parametric point-process model representing the solid phase of LSC-cathodes and fit the parameters of this model to the three exemplary sphere systems extracted from FIB-tomography data. Similar approaches have recently been considered for modeling the ZnO phase in photoactive layers of hybrid polymer-ZnO solar cells and the pore space of graphite electrodes in Li-ion batteries, see [23, 24].

However, a particular challenge in modeling the solid phase of porous materials is to build the stochastic microstructure model in such a way that its realizations consist of one single connected cluster only. To the best of our knowledge, so far there are no models of this kind in literature. In the present paper, the complete connectivity of the simulated LSC phase is achieved by using a suitably chosen class of random geometric graphs, see e.g. [25]. In this way, a stochastic

model is obtained which allows the description and simulation of percolating LSC microstructures for a wide range of sinter temperatures by means of a limited number of parameters. Moreover, our stochastic microstructure model (in combination with physical modeling of transport processes) opens new possibilities for virtual materials design, by identifying rate limiting microstructure effects and by optimizing the parameters for the fabrication of cathodes.

The paper is organized as follows. In Section 2 the fabrication process of the LSC cathodes and the image acquisition by means of FIB-tomography are briefly explained. Subsequently, in Section 3, the structural segmentation of the LSC material is discussed, where the solid phase is represented by a union of moderately overlapping spheres. In Section 4, the stochastic modeling of the sphere systems extracted from FIB-tomography data is described. Last but not least, in Section 5, the microstructure model is validated by the comparison of image characteristics computed for real and simulated data.

2. Experimental Setup

2.1. Materials processing

In a previous paper, see [13], the electrochemical activity is described for the same LSC cathodes as investigated in the present study. Furthermore, in [13] also the fabrication process and the experimental procedure are considered for LSC cathodes with different microstructures, where the fabrication process can be summarized as follows. Powders of $\text{La}_{0.6}\text{Sr}_{0.4}\text{CoO}_{3-\delta}$ were produced by flame spray synthesis, see [26]. The resulting LSC powder is characterized by a bimodal particle size distribution, with a major component of nano-sized particles (15-20 nm) and a minor component of coarser particles ($>1 \mu\text{m}$). The specific surface area measured by BET is $29 \text{ m}^2\text{g}^{-1}$. LSC cathodes are then fabricated by screen printing. For this purpose, pastes with a solid loading of 25 wt % (including LSC and pore former) were prepared. Solsperse3000 (from Avecia) was used as a dispersant and Terpineol (from FLUKA) as solvent. The LSC cathodes tend to form cracks during the sintering and associated shrinkage, which is caused by the high sinter activity of the nano-particles. In order to reduce the crack formation, graphite pore former (Timrex KS4, $D_{50} = 2 \mu\text{m}$) was included in the paste mixture. The samples, which are used in the present study contain 17 wt % of LSC and 8 wt % of graphite. These pastes are screen printed on a $\text{Ce}_{0.8}\text{Gd}_{0.2}\text{O}_{1.9}$ electrolyte substrate, using a $75 \mu\text{m}$ mesh with a thickness of $36 \mu\text{m}$. Sintering in air was then performed at 750, 850 and 950°C .

2.2. Image acquisition

FIB-tomography of the three samples (LSC-750, LSC-850, LSC-950) was performed according to the procedures described in previous papers, see [19, 27, 28, 29]. The sample preparation included polymer impregnation, grinding and polishing. For impregnation of the pores, a polymer system with Araldit BY158 / Aradur 21 (supplied by Huntsman) was used. Mechanical polishing

was performed on textile substrates with diamond suspensions of 6, 3 and 1 μm (MetaDi mono-crystalline diamond suspension, Buehler).

For the FIB-tomography experiments we used a ZEISS NVision 40, which is located at the Electron Microscopy Center of ETH Zürich (EMEZ). The FIB-procedure includes the following steps: 1) Gas assisted metal deposition of 1 μm thick Pt layers. The layer covers a small area of $20 \times 20 \mu\text{m}$ at the location of analysis, in order to protect the surface from ion milling artefacts. 2) Preparation of cubes with edge lengths between 10 to 15 μm . Freestanding cubes are prepared in order to reduce shadowing effects during the acquisition of image stacks (i.e. avoid artificial gray scale gradients). 3) Serial sectioning: Automated acquisition of image stacks is obtained by repeated and alternating execution of erosion (FIB) and imaging (SEM).

During serial sectioning the FIB-slicing is performed with an acceleration voltage of 30 kV and a beam current of 1.5 nA. The ESB detector is used for BSE imaging at low kV (i.e. at 1.2 to 1.8 kV), with an aperture size of 60 μm . The original images consist of 2048×1536 pixel with pixel sizes between 5 to 8 nm. For each sample, 800 to 1200 images are acquired with a slicing distance between 5 and 8 nm (in order to achieve cubic voxels). The resolution in the raw data then reduces to 1024×768 pixel. Hence, the voxel sizes after binning of the raw data is then between 10 and 16 nm. The procedure for the subsequent image analysis consists of a) alignment of the stack, b) cropping of a region of interest (cube sizes between 400 and 900 μm^3), c) noise filtering, d) segmentation, e) visualization and f) quantification.

For the steps a) to e) the software packages Avizo and Fiji are used, see [30] and [31]. For the quantitative analyses in step f) with c-PSD (continuous pore/particle size distribution) and with MIP-PSD (simulation of mercury intrusion porosimetry), we use home-made software, which is developed with Matlab and Java, see [32].

3. Structural Segmentation of Image Data

In this section we describe a technique which allows us to represent the LSC phase by a union of moderately overlapping spheres, where several tools from mathematical image analysis are combined with each other.

After decomposing the LSC phase in disjoint sets by means of a watershed algorithm, each of these sets is represented by a sphere, whose parameters are calculated with the aid of the Hough transform, see also [20]. Furthermore, in order to assure that the extracted sphere system is completely connected, an algorithm is introduced which connects separate clusters of spheres without causing a significant change in the structure. This structural segmentation is exemplarily accomplished for the three FIB-tomography images of LSC cathodes sintered with different temperatures (i.e. LSC-750, LSC-850, LSC-950).

3.1. Transformation to Isotropic Microstructure

It turns out that in LSC-850 and LSC-950 the nanoparticles are formed more like ellipsoids rather than spheres, whereas in LSC-750 most particles

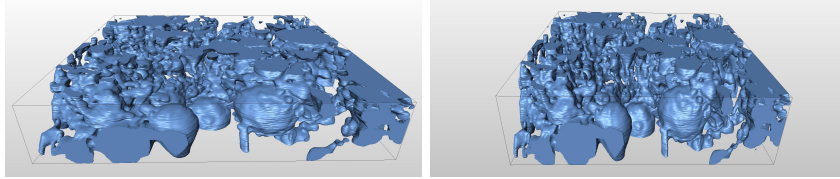


Figure 1: Original (left) and rescaled isotropic (right) 3D images from FIB-tomography for LSC-850

have a spherical shape. A closer inspection shows that the particles in LSC-850 and LSC-950 are compressed in z -direction, see Figure 1 (left). Since isotropic microstructures are much easier to be handled mathematically, the images from LSC-850 and LSC-950 are retransformed to isotropic structures by scaling the z -component accordingly. Segmentation and modeling is then performed on the rescaled isotropic structures, see Figure 1 (right). After rescaling, for all three microstructures we obtain a voxel size of 7.5 nm^3 . Notice that all structural characteristics and model parameters in the present paper are given with respect to this voxel size.

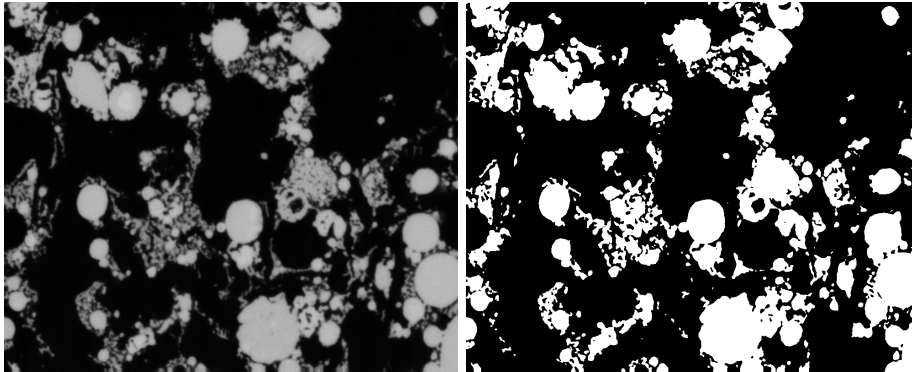


Figure 2: 2D slice (of size $7.4 \times 6.0 \mu\text{m}^2$) of filtered grayscale (left) and binary (right) image of LSC-850

3.2. Binarization

To be brief, the following steps of structural segmentation are explained for LSC-850 only. The segmentation of LSC-750 and LSC-950 is analogous.

At first, the scaled grayscale image $I = \{I(x, y, z), (x, y, z) \in D\}$ gained by FIB-tomography of LSC-850 is converted into a binary image, on which the sphere detection will be arranged. As a preparation step, we apply a median filter of size 3×3 to the grayscale image in order to eliminate noise, see [33]. Then, the filtered grayscale image is binarized by global thresholding with a threshold value of 83, i.e., voxel with grayscale values lower than 83 are set to 0 (black = pore), otherwise to 255 (white = LSC). The threshold has been

chosen manually according to a good optical match, which is adequate because the phase contrast between solid and pore phase (filled with epoxy) is very high, see Figure 2.

3.3. Watershed Transformation

Subsequently, the (solid) foreground $\{(x, y, z) \in D : B(x, y, z) = 1\}$ of the binarized image $B = \{B(x, y, z), (x, y, z) \in D\}$ obtained from I is partitioned into pairwise disjoint sets Z_1, \dots, Z_n . For this purpose the watershed transformation is used, see [34, 35, 36]. The idea of the watershed algorithm is that a grayscale image is interpreted as a topographic relief, where the height of a certain point is given by its grayscale value. Then, metaphorically speaking the relief is flooded, starting at the local minima. In addition, if water from different local minima merge at a certain point we separate the water at this point by a so-called watershed. Thus, we get a partition of the grayscale image into disjoint sets.

Note that the watershed transformation is designed for grayscale images only. However, we do not apply it directly to I , but to the so-called distance transformation of the binary image B , which gives a better separation of the individual objects, see [35]. In the distance transformed image $T = \{T(x, y, z), (x, y, z) \in D\}$ we associate each voxel $(x, y, z) \in D$ with its shortest distance $T(x, y, z)$ to the background phase. This can be done very efficiently using e.g. the algorithm proposed in [41]. The resulting grayscale image T is then inverted such that it fits better to the watershed framework, i.e., we consider the image T' given by

$$T'(x, y, z) = \max_{(x', y', z') \in D} T(x', y', z') - T(x, y, z), \quad (x, y, z) \in D.$$

The result of the watershed transformation applied to T' is a subdivision of the domain D into disjoint sets $Z'_1, \dots, Z'_n \subset D$. The binary image displaying the union of boundaries $\partial Z'_1 \cup \dots \cup \partial Z'_n$ between the sets Z'_1, \dots, Z'_n , so-called watershed lines, is denoted by W , see Figure 3 (left). We 'subtract' W from B , where the resulting binary image shows the partitioning of the solid phase of image B into disjoint sets Z_1, \dots, Z_n , see Figure 3 (right).

3.4. Hough Transform

In the next step we represent each of the components Z_1, \dots, Z_n of the solid phase derived in Section 3.3 by one spherical object. Note that the Hough transform is a suitable technique to detect geometrical objects, which can be uniquely described by a few parameters, see e.g. [37] and [38]. In our case, spheres are uniquely determined by their midpoint (x, y, z) and radius r .

The key idea of the Hough transform is to build up the Hough spaces corresponding to the sets Z_1, \dots, Z_n , whose elements are 4-dimensional vectors (x, y, z, r) each representing a sphere. For each $i = 1, \dots, n$, the possible values of (x, y, z) are given by all points contained in Z_i and the values of r are in $\mathcal{R} = \{1, \dots, r_{max}\}$, where the maximum radius $r_{max} = 300$ is chosen manually. Then, denoting by $A(x, y, z, r)$ the number of voxel which simultaneously belong to the surface of the discretized sphere (x, y, z, r) and the surface of Z_i ,

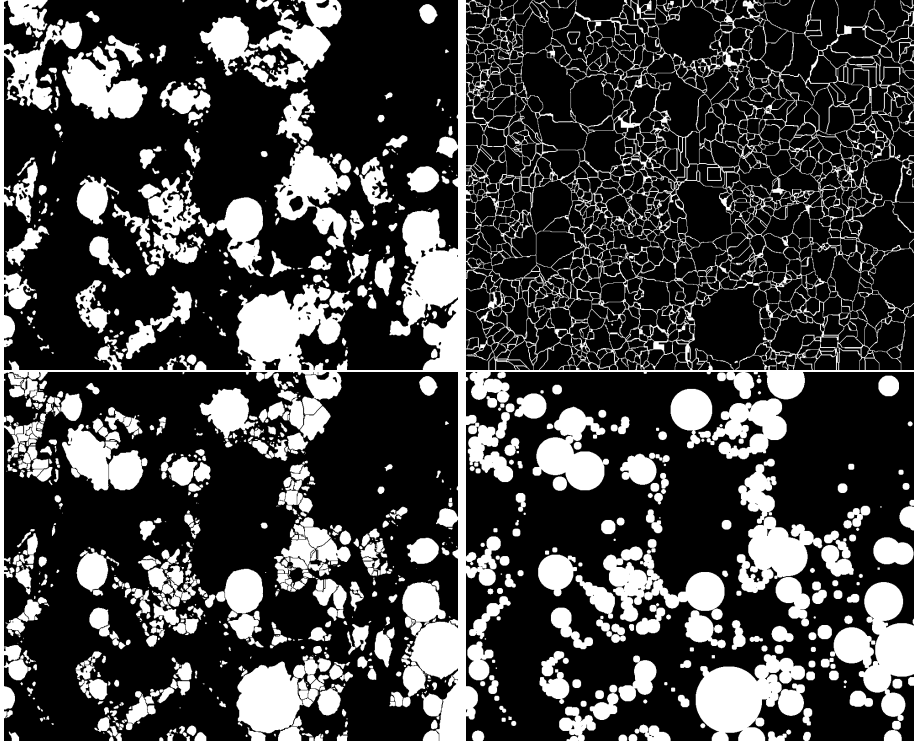


Figure 3: Binary image (top left), watershed lines (top right), the partition of the solid phase in B (bottom left) obtained by the watershed transform of T' and the sphere representation by means of the Hough transform (bottom right) on a observation window of size $7.4 \times 6.0 \mu m^2$

the result of the Hough transformation for the set Z_i is a sphere (x, y, z, r) such that $A(x, y, z, r) \geq A(x', y', z', r')$ for all $(x', y', z') \in Z_i$ and $r' \in \mathcal{R}$.

A comparison of the binary image B and its sphere representation B' after applying the Hough transform is given in Figures 3 (right) and 4, which shows that the 3D structures of B and B' are in good accordance. Merely, the volume fraction of the foreground phase of B' is slightly smaller than that of B .

3.5. Improvement of Connectivity and Volume Fraction

The LSC particles in the porous electrodes form a grain-supported texture, where all particles are in contact with each other. This means that also in the segmented image the solid phase should be perfectly connected, i.e., each sphere has to be connected to another one. This requirement can not directly be ensured by the sphere extraction algorithm described above. Thus, in order to achieve complete connectivity of the sphere system, the following iterative procedure is proposed, which changes the structure of the original sphere system only marginally: 1) Determine the clusters of connected spheres and allocate the corresponding cluster number to each sphere by using the algorithm described

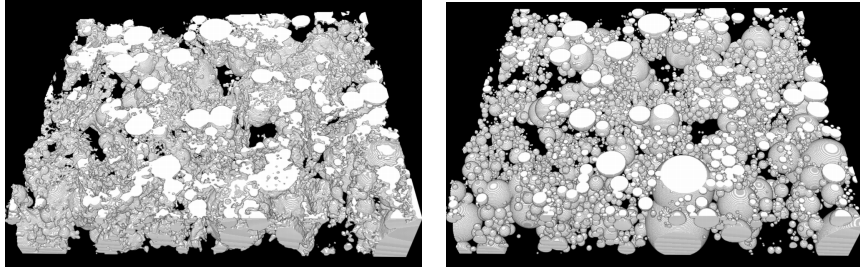


Figure 4: 3D cutout (of size $7.4 \times 6.0 \times 1.1 \mu\text{m}^3$) of the binary image B before (left) and after (right) applying the sphere detection algorithm

in [39]. 2) Find the pair of spheres $(x_{i_1}, y_{i_1}, z_{i_1}, r_{i_1}), (x_{i_2}, y_{i_2}, z_{i_2}, r_{i_2})$ which belong to different clusters and have the smallest Euclidean distance d from each other. 3a) If $d \leq 2$ and $\max\{r_{i_1}, r_{i_2}\} < 20$, the radii are increased such that the two spheres overlap, i.e., the new radii $r'_{i_1} = r_{i_1} + d/2$ and $r'_{i_2} = r_{i_2} + d/2$ are considered. 3b) Otherwise, a new sphere (x, y, z, r) is put such that $x = x_{i_1} + s \cdot (x_{i_2} - x_{i_1}), y = y_{i_1} + s \cdot (y_{i_2} - y_{i_1}), z = z_{i_1} + s \cdot (z_{i_2} - z_{i_1})$ and $r = d/2 + 0.1$, where $s = (r_{i_1} + d/2) / (|x_{i_1} - x_{i_2}| + |y_{i_1} - y_{i_2}| + |z_{i_1} - z_{i_2}|)$. 4) Repeat steps 1 to 3 until only one cluster of spheres remains.

For the considered image data of LSC-850, the volume fraction of the foreground phase of B' has been increased from 30.14% to 30.96% by applying the iterative procedure described above, i.e., the structure of the sphere system has been changed only marginally in order to achieve complete connectivity.

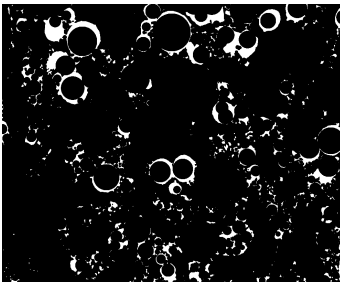


Figure 5: Difference image $B - B''$ (of size $7.4 \times 6.0 \mu\text{m}^2$), illustrating that the radii of spheres in B'' are slightly underestimated

Finally, the volume fraction (30.96%) of the completely connected sphere system, denoted by B'' in the following, is fitted to the volume fraction (35.21%) of the binary image B . For this reason, we examine the difference image $B - B''$. In view of the homogeneous distribution of non-detected foreground voxels of B , see Figure 5, we can assume that in the sphere system B'' the radii of the detected spheres are slightly underestimated. Thus, the radii of all spheres in B'' are increased by 0.8, leading to a volume fraction of 35.36%, where this final sphere representation is denoted by R .

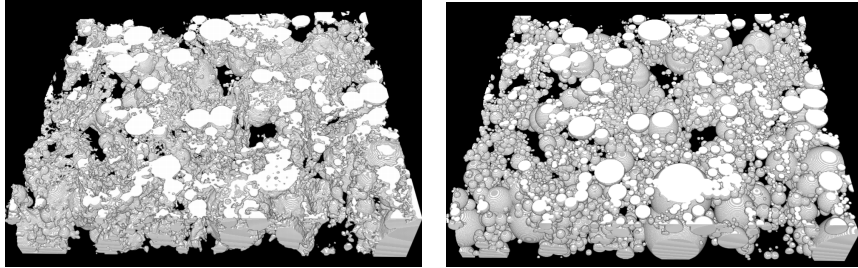


Figure 6: 3D cutout (of size $7.4 \times 6.0 \times 1.1 \mu\text{m}^3$) of binary image B (left) and sphere system R (right)

It turns out that not only the volume fractions of the foreground phases of B and R nicely coincide, see Figure 6. A very good agreement is also observed for further image characteristics of B and R .

3.6. Structural Analysis of Sphere Representation

In order to analyze if the sphere system R represents the most important properties of the real microstructure (as captured by FIB-tomography), several structural characteristics of R and the original binary image B are calculated and compared to each other. In particular, the spherical contact distribution functions $H, \tilde{H} : [0, \infty) \rightarrow [0, 1]$ of background (pore) and foreground (solid) phase are computed, where $H(t)$ is the probability that the minimum distance from a randomly chosen point of the pore phase to the solid phase is not larger than $t > 0$. Similarly, $\tilde{H}(t)$ is the probability that the minimum distance from a randomly chosen point of the solid phase to the pore phase is not larger than t . It turns out that the spherical contact distribution functions H and \tilde{H} obtained from B and R , respectively, are nearly identical, see Figure 7.

As further structural characteristics, the continuous particle and pore size distributions $P, \tilde{P} : [0, \infty) \rightarrow [0, 1]$ have been calculated for B and R , where $P(t)$ is the volume fraction, which can be covered by spheres with center belonging to the foreground phase, and radius t , such that these spheres have no intersection with the background phase. The value $\tilde{P}(t)$ of the continuous pore size distribution is defined analogously, but now from the perspective of the background phase, see [32]. Note that the continuous particle and pore size distributions P and \tilde{P} computed for B and R , respectively, are very similar, see Figure 8.

Thus, it is reasonable to consider the sphere representation R as the data basis for our stochastic microstructure model of LSC cathodes.

4. Stochastic Microstructure Model

In this section we present our approach to stochastic modeling of the 3D microstructure of LSC cathodes, where we fit the model parameters to three different LSC cathodes produced with sinter temperatures of 750, 850 and 950°C,

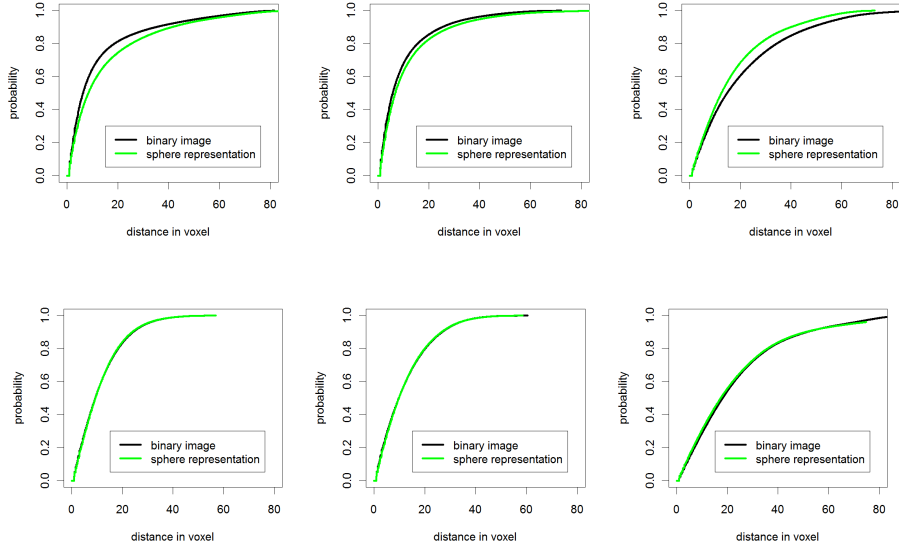


Figure 7: Spherical contact distribution functions H (top row), \tilde{H} (bottom row) computed for LSC-750 (left), LSC-850 (center) and LSC-950 (right)

respectively. A particular challenge in modeling the solid phase of LSC electrodes is to construct the model in such a way that with probability 1 its realizations consist of one single cluster only.

The basic idea is to consider the sphere systems, whose extraction from FIB-tomography images has been described in Section 3, as realizations of random marked point processes, which can be interpreted as random germ-grain models with spherical grains, i.e. random sphere systems. To achieve the goal that the random sphere systems are completely connected with probability 1, we introduce a suitably chosen class of random geometric graphs, being a modified version of so-called relative neighborhood graphs. The vertices of the graphs will be the midpoints of the spheres to be constructed, whereas their edges correspond to pairs of (moderately) overlapping spheres.

Note that the model type described above will be the same for all three LSC electrodes considered in this paper. Just the specification of the model parameters is different in each case. This means in particular that our stochastic microstructure model can be used for computer-based scenario analyses with the general objective of developing improved materials and technologies for LSC electrodes.

4.1. Modeling of Sphere Midpoints

We first introduce a point-process model, which accurately describes the geometrically complex patterns of sphere midpoints as observed in the sphere

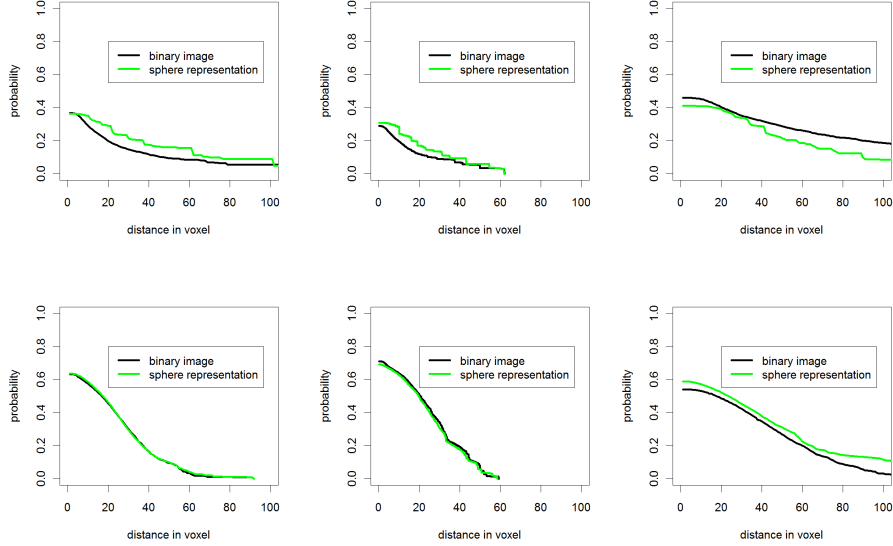


Figure 8: Continuous particle (top row) and pore size distribution (bottom row) computed for LSC-750 (left), LSC-850 (center) and LSC-950 (right)

systems extracted from FIB-tomography data for LSC-750, LSC-850 and LSC-950. For details regarding marked point processes as well as their statistical inference and simulation, we refer e.g. to [21, 22].

In order to appropriately select the model type for the patterns of sphere midpoints extracted in Section 3, the following key properties of these point patterns should be taken into account: 1) There are clusters of points in the neighborhood of large spheres, see Figure 9 (left). 2) There exist large regions of empty space, where are no points at all, see Figure 9 (right). The latter property can be explained by the manufacturing process described in Section 2.

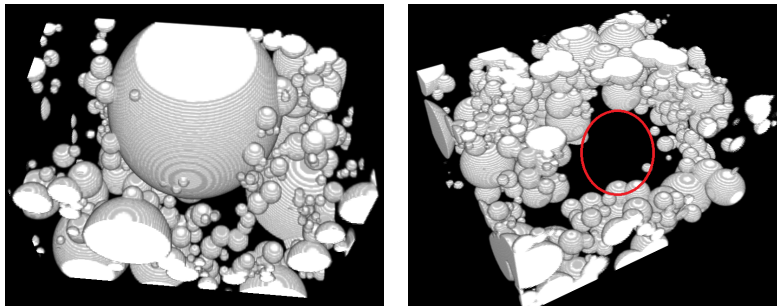


Figure 9: Key properties of extracted sphere systems: clusters of small spheres (left) and large regions of empty space (right)

4.1.1. Large Spheres

To begin with, we consider the midpoints of those spheres whose radii are larger than a certain threshold $t_1 > 0$. The point patterns of these midpoints are modeled by a Matérn hardcore point processes $\{S_n\}$ in \mathbb{R}^3 with some intensity $\lambda_h > 0$ and hardcore radius $r_h > 0$, see [21]. Furthermore, the radii of large spheres are modeled by sequences of independent and identically distributed random variables $\{M_n\}$, which are independent of $\{S_n\}$. The distribution of M_n belongs to a class of (shifted and truncated) inverse Gaussian distributions. More precisely, M_n has an inverse Gaussian distribution $\text{IG}(\mu_1, \mu_2, t_1, t_2)$ with parameters $\mu_1, \mu_2 > 0$, which is shifted to the right by the threshold $t_1 > 0$ introduced above and truncated at some $t_2 > t_1$, i.e., the random variables M_n take their values in the interval $[t_1, t_2]$ in view of the fact that the radii can not become arbitrarily large as the production process yields a bounded size of the LSC particles.

The marked point process $\{S_n, M_n\}$ then yields the random system of large spheres $\Xi = \bigcup_{n=1}^{\infty} b(S_n, M_n)$, where $b(x, r) = \{y \in \mathbb{R}^3 : |x - y| \leq r\}$ denotes the sphere with midpoint $x \in \mathbb{R}^3$ and radius $r > 0$.

4.1.2. Large Empty Regions

In the next step the large empty regions are included into our microstructure model by considering the random set $\Xi' = \bigcup_{n=1}^{\infty} b(P_n, r_0)$, where $r_0 > 0$ is some constant and $\{P_n\}$ is a (conditional) Poisson point process in the complementary set $(\Xi \oplus b(o, r_0))^c$ with some intensity $\lambda > 0$. Note that by definition it holds that $\Xi' \cap \Xi = \emptyset$, i.e., the random set Ξ' can be interpreted as union of forbidden zones for midpoints of spheres.

4.1.3. Remaining Sphere Midpoints

The midpoints of the remaining spheres, i.e. spheres with radii smaller than t_1 , are modeled by clustered Coxian point processes, see [21], under the condition that the random sets Ξ (union of large spheres) and Ξ' (empty space) are given.

Note that the midpoints of small spheres should neither be contained in the union set Ξ of large spheres, nor in the empty space Ξ' . Furthermore, the midpoints of small spheres are clustered and their intensity increases with decreasing distance to the set Ξ . Thus, the clustered Cox processes of midpoints of small spheres are built as follows. First, for some constant $\lambda_c > 0$, we consider an inhomogeneous Poisson point process $\{\tilde{P}_n\}$ (of cluster centers) in the complementary set $(\Xi \cup \Xi')^c$ with intensity field $\lambda_p(\cdot) = \lambda(\cdot)/\lambda_c$, where

$$\lambda(x) = \begin{cases} a \cdot (\min\{|x - y| : y \in \Xi\})^b & \text{if } x \notin \Xi \cup \Xi', \\ 0 & \text{if } x \in \Xi \cup \Xi', \end{cases} \quad (1)$$

and $a, b \in \mathbb{R}$ are some parameters. Then, within the union set $\bigcup_{n=1}^{\infty} b(\tilde{P}_n, r_c)$ of spheres with some radius $r_c > 0$, intersected by the set $(\Xi \cup \Xi')^c$, a homogeneous Poisson process $\{\tilde{S}_n\}$ with intensity λ_c is considered, which models the midpoints of small spheres.

4.1.4. Model Fitting

The stochastic model of sphere midpoints introduced in Sections 4.1.1–4.1.3 has 12 parameters: $\lambda_h, r_h, \mu_1, \mu_2, t_1, t_2, a, b, \lambda_c, r_c, \lambda_s$ and r_0 .

The parameter λ_h can easily be estimated by $\hat{\lambda}_h = \#\{S_n : S_n \in W\}/|W|$, where $\#\{S_n : S_n \in W\}$ is the number of midpoints of large spheres in some sampling window $W \subset \mathbb{R}^3$ and $|W|$ denotes the volume of W . The hardcore distance r_h is estimated as the minimum distance $\hat{r}_h = \min_{n \neq m} \{|S_n - S_m|\}$ observed between two points of $\{S_n\}$. Furthermore, μ_1, μ_2 are estimated by means of the maximum likelihood method.

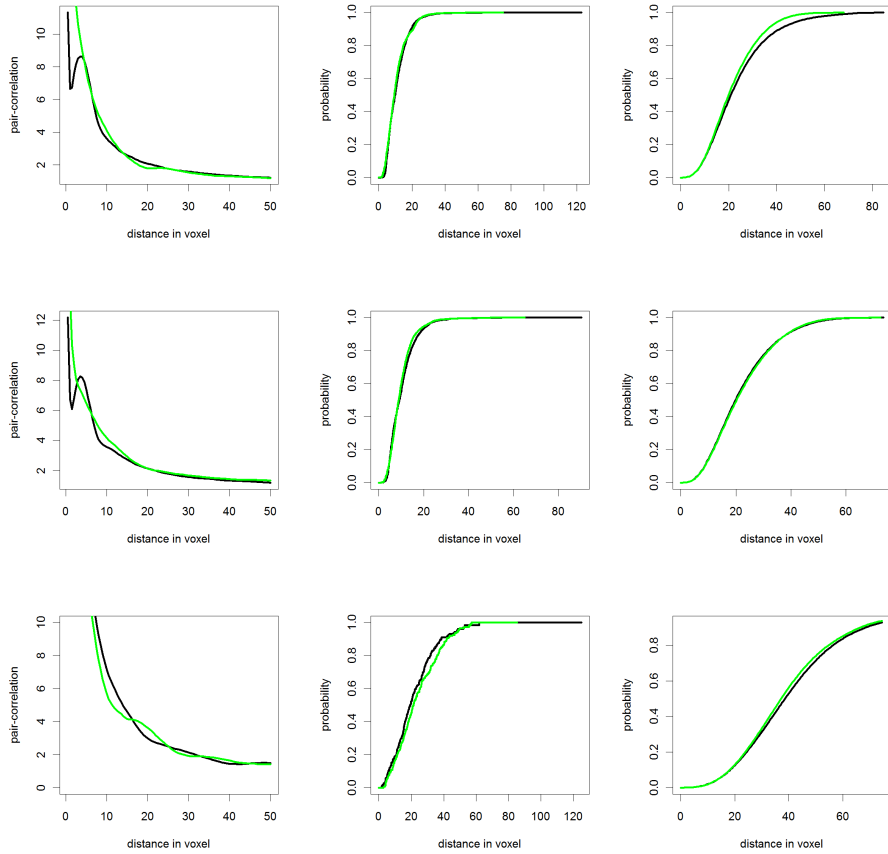


Figure 10: Pair correlation function (left), nearest-neighbor-distance distribution function (center) and spherical contact distribution function (right) for extracted (black) and simulated sphere midpoints for LSC-750 (top), LSC-850 (center) and LSC-950 (bottom)

The (unscaled) intensity field $\lambda(x)$ at location $x \in \mathbb{R}^3$, introduced in (1), depends on the distance $d_{\Xi}(x) = \min\{|x - y| : y \in \Xi\}$ between x and the union set of spheres Ξ , where we put $\lambda(x) = 0$ if $x \in \Xi \cup \Xi'$. Thus, the value of $\lambda(x)$ at locations $x \notin \Xi \cup \Xi'$ can be estimated by analyzing the intensity of sphere midpoints in the sets $B_i^{\Xi} = \{x \in \mathbb{R}^3 : d_{\Xi}(x) \in (2i, 2i + 2]\}$ for $i = 0, 1, 2, \dots$. In particular, for any $i = 0, 1, 2, \dots$, the intensity $\lambda(x)$ at locations $x \in B_i^{\Xi}$ can be estimated by

$$\hat{\lambda}(x) = \frac{\#\{\tilde{S}_n : \tilde{S}_n \in B_i^{\Xi}\}}{|B_i^{\Xi}|}.$$

Then, inserting $\hat{\lambda}(x)$ into (1), estimates \hat{a} and \hat{b} for a and b can be computed using least squares methods of non-linear regression analysis.

The parameters t_1, t_2 are estimated manually taking into account the empirical distributions of radii of the sphere systems extracted in Section 3 from FIB-tomography data. The remaining four parameters λ_c, r_c, λ , and r_0 are estimated by the so-called minimum contrast method, where the following cost function has been considered:

$$L(\lambda_c, r_c, \lambda, r_0) = \int_{r_1}^{r_2} (|N(r) - N_{\lambda_c, r_c, \lambda, r_0}(r)| + |g(r) - g_{\lambda_c, r_c, \lambda, r_0}(r)|) dr. \quad (2)$$

Here, $N, N_{\lambda_c, r_c, \lambda, r_0}$ and $g, g_{\lambda_c, r_c, \lambda, r_0}$ denote the nearest-neighbor-distance distribution function and the pair correlation function, see [21], computed for the midpoints of spheres which have been extracted from the FIB-SEM images and for point patterns simulated from the point-process model described above, respectively, and the constants r_1, r_2 in (2) are appropriately chosen integration limits. A vector $(\hat{\lambda}_c, \hat{r}_c, \hat{\lambda}, \hat{r}_0)$ such that $L(\hat{\lambda}_c, \hat{r}_c, \hat{\lambda}, \hat{r}_0) \leq L(\lambda_c, r_c, \lambda, r_0)$ holds for all admissible values of $(\lambda_c, r_c, \lambda, r_0)$ is called a minimum contrast estimator for $(\lambda_c, r_c, \lambda, r_0)$.

The numerical values of the fitted parameters which have been obtained for LSC-750, LSC-850 and LSC-950 are given in Table 1. Furthermore, Figure 10 shows that not only the nearest-neighbor-distance distribution functions and the pair correlation functions computed for the FIB-SEM images and for the point patterns simulated from the fitted point-process models coincide nicely. This is also true for the spherical contact distribution function, see Figure 10, which has not been used for model fitting.

4.2. Graph-based Modeling of Connectivity

Note that the sphere representation R derived in Section 3 can be seen as a completely connected graph $G_R = (V_R, E_R)$, where the vertex set V_R is the set of sphere midpoints, the edge set E_R corresponds to pairs of overlapping spheres, and, in addition, the vertices of G_R are weighted by the radii of spheres. Our goal is now to determine a mathematical rule for setting edges such that 1) the resulting edge set has similar structural properties as E_R , given the vertex set V_R , and 2) considering the realizations of the point-process model introduced in Section 4.1 as vertex sets, the resulting (infinite) graphs should be completely connected with probability 1.

Table 1: Fitted parameters of point-process model for different sinter temperatures computed with respect to the voxel size of 7.5 nm^3

	LSC-750	LSC-850	LSC-950
$\widehat{\lambda}_h$	0.00000227	0.0000013	0.00000082
\widehat{r}_h	19.95	22.93	20.22
$\widehat{\mu}_1$	6.24	8.38	12.48
$\widehat{\mu}_2$	2.07	2.56	6.05
\widehat{t}_1	20	20	30
\widehat{t}_2	300	300	300
$\widehat{\lambda}$	0.0005	0.000037	0.005
\widehat{r}_0	11	22	6
\widehat{a}	0.00011	0.00013	0.000027
\widehat{b}	-0.3883	-0.3187	-0.6447
$\widehat{\lambda}_c$	0.000087	0.00014	0.000023
\widehat{r}_c	14	12	25

Regarding the first criterion (of structural similarity) mentioned above, a connection rule is constructed such that there is a high accordance in the distributions of the edge length and the coordination number (i.e. the number of edges emanating from a vertex). It turns out that a modified version of so-called relative neighborhood graphs fulfills these requirements. Furthermore, it can be shown that with probability 1 this approach leads to completely connected graphs if the random vertex set is given by the point-process model introduced in Section 4.1.

4.2.1. Modified Relative Neighborhood Graphs

For a given set of vertices $V = \{v_1, v_2, \dots\} \in \mathbb{R}^3$, the relative neighborhood graph (RNG) is defined as follows, see e.g. [40]. Two vertices $u, v \in V$ are connected by an edge if and only if

$$d(u, v) \leq \max\{d(v, v'), d(v', u)\} \quad \text{for all } v' \in V \setminus \{u, v\}, \quad (3)$$

where $d(u, v) = |u - v|$ denotes the Euclidean distance between u and v .

It is not difficult to see that the RNG corresponding to a finite vertex set is completely connected. Thus, in principle, the *RNG* would be an appropriate model for the edge set of G_R , given the vertex set V_R . However, in the graph G_R corresponding to R we observe vertices with huge nearest-neighbor distances and, in addition, with very large coordination numbers (up to 36). These features can not be comprehended by the RNG. Thus, in order to get a good fit to the empirical distributions of edge lengths and coordination numbers of G_R , we modify the *RNG* by substituting the Euclidean distance in (3) for new distance functions $d_0, d'_0 : \mathbb{R}^3 \times \mathbb{R}^3 \rightarrow [0, \infty)$ defined as follows.

For each vertex $v \in V$, let $w(v) = \min\{d(u, v) : u \in V \setminus \{v\}\}$ denote the

nearest-neighbor distance of v . Then, for any $u, v \in V$, we put

$$d_0(u, v) = \begin{cases} \frac{d(u, v)}{\max\{w(u), w(v)\}^\alpha} & \text{if } \max\{w(u), w(v)\} > c, \\ d(u, v) & \text{if } \max\{w(u), w(v)\} \leq c, \end{cases} \quad (4)$$

and

$$d'_0(u, v) = \begin{cases} d_0(u, v) & \text{if } \frac{d(u, v)}{w(u) + w(v)} < \delta, \\ \infty & \text{otherwise,} \end{cases} \quad (5)$$

where $\alpha \in \mathbb{R}$ and $c, \delta > 0$ are some constants. The resulting modified RNG with vertex set V is denoted by $G_{\alpha, c}(V)$ and $G_{\alpha, c, \delta}(V)$, respectively, where we do not put an edge in $G_{\alpha, c, \delta}(V)$ connecting $u, v \in V$ if $d'_0(u, v) = \infty$.

Note that the large coordination numbers appearing in G_R in combination with large nearest-neighbor distances are reasonable because due to the structural segmentation considered in Section 3, it happens that many small spheres are attached to large ones, see Figure 12. This provides star-shaped regions within the graph G_R , which do not appear in the relative neighborhood graph if the Euclidean distance between vertices is considered. But, by means of the distance function d'_0 , the modified RNG $G_{\alpha, c, \delta}(V_R)$ can generate such star-shaped regions for $\alpha > 0$, because then a vertex $v \in V_R$ with a large Euclidean nearest-neighbor distance $w(v)$ has a smaller nearest-neighbor distance with respect to d'_0 . As a result the coordination number of these vertices increases, while in regions with relatively densely packed vertices the modified RNG $G_{\alpha, c, \delta}(V_R)$ is built in the classical way because $d_0(u, v) = d(u, v)$ if $\max\{w(u), w(v)\} \leq c$.

Using proving techniques which have recently been developed in [25], it is not difficult to show that the graph $G_{\alpha, c}(X)$ with respect to the distance function d_0 defined in (4) is completely connected with probability 1 if the (random) vertex set X is given by the union $X = \{S_n\} \cup \{\tilde{S}_n\}$ of the point processes $\{S_n\}$ and $\{\tilde{S}_n\}$ introduced in Section 4.1.

Unfortunately, the graph $G_{\alpha, c}(V_R)$ with distance function d_0 still contains very long edges connecting different clusters of points. Since putting an edge (u, v) connecting $u, v \in V_R$ means that the corresponding spheres $b(u, r_u)$ and $b(v, r_v)$ to be constructed should intersect each other, i.e., the radii r_u, r_v have to be very large. Thus, these large spheres influence and bias the resulting sphere system to a high degree. In order to avoid this type of phenomena, we only set an edge connecting the vertices $u, v \in V_R$ if the Euclidean distance $d(u, v)$ is not too large with respect to the nearest-neighbor distances $w(u)$ and $w(v)$, i.e., $d(u, v) < \delta(w(u) + w(v))$ for some $\delta > 0$. However, under this additional condition the complete connectivity of the random graph $G_{\alpha, c, \delta}(X)$ can not be ensured anymore for $X = \{S_n\} \cup \{\tilde{S}_n\}$.

We solve this problem by adding a few more edges to $G_{\alpha, c, \delta}(V_R)$. Since it is desirable that the lengths of these additional edges are as small as possible, the so-called creek-crossing graph $G_{\alpha, c}^{(n)}(V_R)$ with respect to the distance function d_0 is considered for some $n > 1$ which is defined as follows. For any vertex set

Table 2: Fitted parameters of connectivity model for different sinter temperatures computed with respect to voxel size 7.5 nm^3

	LSC-750	LSC-850	LSC-950
α	2.00	1.00	1.00
c	36.00	1.00	11.00
δ	0.97	0.97	0.95

$V = \{v_1, v_2, \dots\} \in \mathbb{R}^3$, two vertices $u, v \in V$ are connected in $G_{\alpha,c}^{(n)}(V)$ if and only if there exists no integer $m \leq n$ and vertices $u = v_0, v_1, \dots, v_m = v \in V$ with $d_0(v_i, v_{i+1}) < d_0(u, v)$ for all $i \in \{0, \dots, m-1\}$, see [25].

Using again the proving techniques developed in [25], it can be shown that $G_{\alpha,c}^{(n)}(X)$ is connected for each $n > 1$ with probability 1. We therefore consider the graph $G_{\alpha,c,\delta}^{(n)}(V_R) = G_{\alpha,c,\delta}(V_R) \cup G_{\alpha,c}^{(n)}(V_R)$ as our connectivity model, where $n > 1$ is chosen a very large (fixed) integer. More precisely, if $G_{\alpha,c,\delta}^{(n)}(V_R)$ is simulated on a bounded observation window W , then we put n equal to the number of vertices in $V_R \cap W$ and thus $G_{\alpha,c}^{(n)}(V_R)$ is equivalent with the minimum spanning tree.

4.2.2. Model Fitting

Using the minimum-contrast method, the parameters α, c, δ of $G_{\alpha,c,\delta}^{(n)}(V_R)$ are fitted to the sphere systems extracted in Section 3 for LSC-750, LSC-850 and LSC-950. The following cost function is used:

$$L(\alpha, c, \delta) = \sup_{r \leq r_{\max}} |D(r) - D_{\alpha,c,\delta}(r)| + |K(r) - K_{\alpha,c,\delta}(r)| + \left(1 - \frac{|E_R \cap E_{\alpha,c,\delta}|}{|E_R|}\right),$$

where $r_{\max} > 0$ is a sufficiently large constant, and $D, D_{\alpha,c,\delta}$ and $K, K_{\alpha,c,\delta}$ are the empirical distribution functions of edge lengths and coordination numbers computed for the graphs $G_R = (V_R, E_R)$ and $G_{\alpha,c,\delta}^{(n)}(V_R)$, respectively. Furthermore, $|E_R \cap E_{\alpha,c,\delta}|$ denotes the number of edges which simultaneously occur in the graphs $G_R = (V_R, E_R)$ and $G_{\alpha,c,\delta}^{(n)}(V_R)$.

The numerical values of the fitted parameters which have been obtained for LSC-750, LSC-850 and LSC-950 are given in Table 2. Figure 11 shows that the distributions of edge lengths and coordination numbers, respectively, of the graphs $G_R = (V_R, E_R)$ and $G_{\alpha,c,\delta}^{(n)}(V_R)$ nicely coincide for LSC-750, LSC-850 and LSC-950. Furthermore, Figure 12 shows exemplarily for LSC-850 that there is a good visual agreement between the sphere system R extracted from FIB-tomography data, the graph $G_R = (V_R, E_R)$ corresponding to R , the modeled graph $G_{\alpha,c,\delta}^{(n)}(V_R)$ with the same vertex set V_R as in G_R , and the random graph $G_{\alpha,c,\delta}^{(n)}(X)$, where $X = \{S_n\} \cup \{\tilde{S}_n\}$ is the point process introduced in Section 4.1.

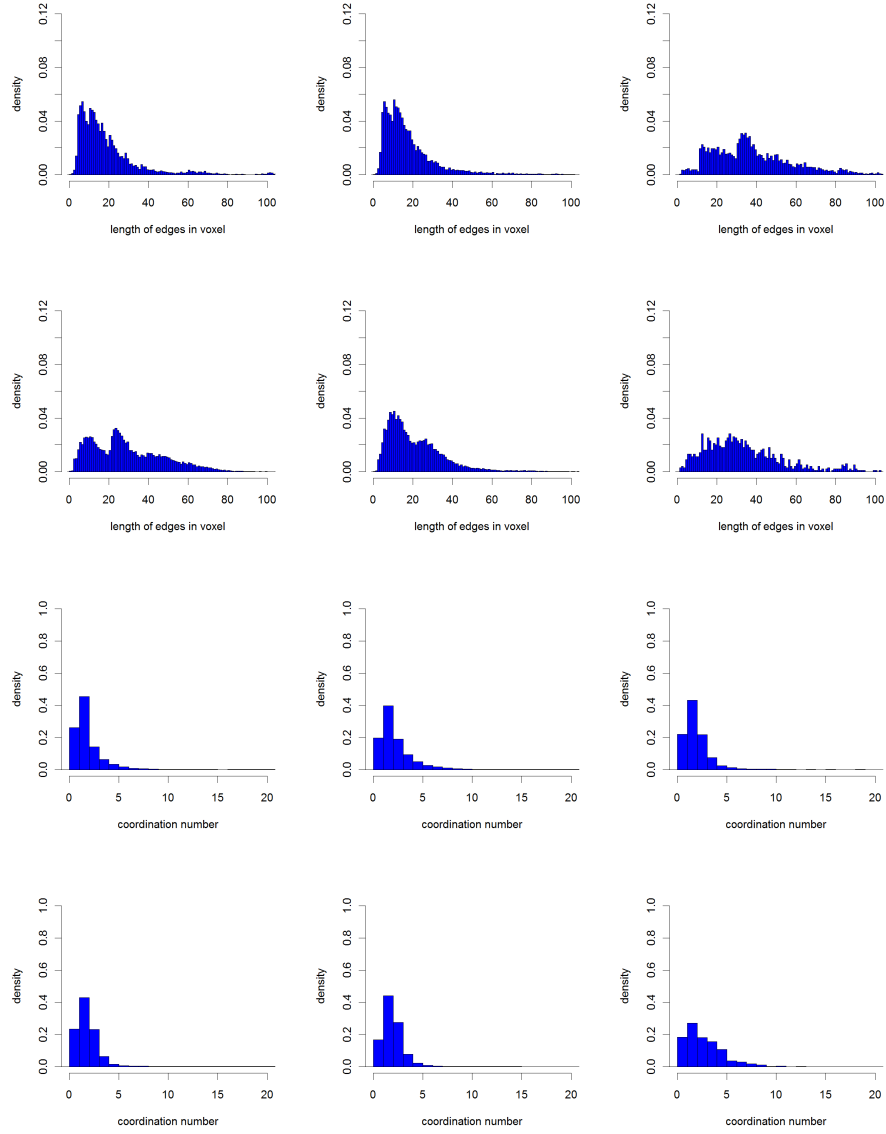


Figure 11: Distributions of edge lengths in $G_R = (V_R, E_R)$ (first row) and $G_{\alpha,c,\delta}^{(n)}(V_R)$ (second row), and distributions of coordination number in $G_R = (V_R, E_R)$ (third row) and $G_{\alpha,c,\delta}^{(n)}(V_R)$ (fourth row) for LSC-750 (first column), LSC-850 (second column) and LSC-950 (third column)

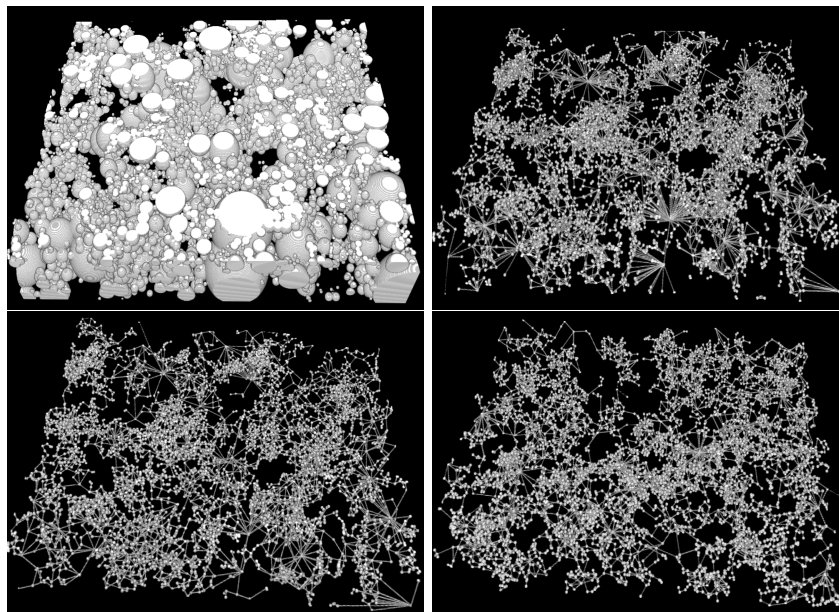


Figure 12: Sphere system R and graph $G_R = (V_R, E_R)$ (top), modeled graph $G_{\alpha, c, \delta}^{(n)}(V_R)$ with the same vertex set V_R (bottom left) and random graph $G_{\alpha, c, \delta}^{(n)}(X)$ (bottom right) on a observation window of size $7.4 \times 6.0 \times 1.1 \mu m^3$

4.3. Retransformation into Sphere System – Modeling of Radii

Using the point process $X = \{S_n\} \cup \{\tilde{S}_n\}$ and the random graph $G_{\alpha,c,\delta}^{(n)}(X)$, we now describe how the radii of the random sphere system to be constructed are determined. The radii of the large spheres, i.e. spheres with radii larger than t_1 , have already been modeled in Section 4.1. Thus, only the radii of the small spheres, i.e. spheres with radii smaller than t_1 , have to be determined. This is done in the following way.

First, the radii of all small spheres are put equal to t_1 . Then, each edge $(u, v) \in G_{\alpha,c,\delta}^{(n)}(X)$ such that the spheres around the corresponding vertices $u, v \in X$ do not overlap, is split into two (sub-) edges of equal length by cutting the edge (u, v) at $(u + v)/2$. Subsequently, a sphere with radius t_1 and midpoint at the new vertex $(u + v)/2$ is added. This splitting of edges and adding of spheres is repeated until no edges are left such that the spheres around the corresponding vertices do not overlap.

Now, the radii of those small spheres are simultaneously decreased by some small value $\varepsilon > 0$ such that the volumes of their overlappings with all direct neighboring spheres do not become smaller than a certain threshold value $\rho > 0$. Otherwise, the radius is not decreased. In our case we choose $\varepsilon = 0.01$.

The resulting random system of (moderately) overlapping spheres is denoted by $\{B_n\}$. It is completely connected, where the parameter ρ is chosen such that the volume fraction of the union $\bigcup_{n=1}^{\infty} B_n$ is equal to the volume fraction of the LSC phase in the binary image B considered in Section 3. This leads to the values $\rho = 0.07$, $\rho = 0.03$ and $\rho = 0.08$ for LSC-750, LSC-850 and LSC-950, respectively.

4.4. Fitting of Specific Surface Area

The union set $\bigcup_{n=1}^{\infty} B_n$ of the random sphere system $\{B_n\}$ of (moderately) overlapping spheres introduced in Section 4.3 fits the volume fraction of the LSC phase quite well. Furthermore, the connectivity properties of $\bigcup_{n=1}^{\infty} B_n$ are similar to those of the LSC phase. But the specific surface area of the LSC phase is underestimated by $\bigcup_{n=1}^{\infty} B_n$, in particular for the finest morphology of LSC-750, see Figure 14. The reason for this is that the sphere is the geometrical object with the smallest possible specific surface area.

We thus develop an algorithm for roughening the surface of the random set $\bigcup_{n=1}^{\infty} B_n$ in order to increase its specific surface area, without changing the volume fraction nor destroying the connectivity of $\bigcup_{n=1}^{\infty} B_n$. For this purpose, we consider a random marked point process $\{P_i, M_i\}$ on the surface $\partial(\bigcup_{n=1}^{\infty} B_n)$ of $\bigcup_{n=1}^{\infty} B_n$, where the points $P_i \in \partial(\bigcup_{n=1}^{\infty} B_n)$ indicate the locations for adding/removing small (spherically shaped) ‚particles‘ at the surface of $\bigcup_{n=1}^{\infty} B_n$ and the absolute values $|M_i|$ of the marks $M_i \in \mathbb{R}$ indicate the size of these particles. More precisely, a random sphere $b(P_i, |M_i|)$ with midpoint P_i located on $\partial(\bigcup_{n=1}^{\infty} B_n)$ is either added to $\bigcup_{n=1}^{\infty} B_n$, or the intersection $\bigcup_{n=1}^{\infty} B_n \cap b(P_i, |M_i|)$ is removed. Thus, the ‚roughened‘ microstructure model of the LSC phase is given by $(\bigcup_{n=1}^{\infty} B_n \cup \bigcup_{i: M_i > 0} b(P_i, M_i)) \setminus \bigcup_{i: M_i < 0} b(P_i, |M_i|)$.

Regarding the random marked point process $\{P_i, M_i\}$, we assume that $\{P_i\}$ is some kind of dominance competition point process on the surface $\partial(\bigcup_{n=1}^{\infty} B_n)$ of $\bigcup_{n=1}^{\infty} B_n$ as described in [21], where $\{P_i\}$ is obtained by the following thinning procedure of a homogeneous Poisson process $\{P'_i\}$ with some intensity $\gamma > 0$ on $\partial(\bigcup_{n=1}^{\infty} B_n)$. To control the distances between pairs of points, every 'Poisson point' P'_i is associated with a suitably chosen random mark M'_i , where $\{M'_i\}$ is a sequence of independent and identically distributed random variables. The point P'_i 'survives' if and only if there is no other point P'_j such that $M'_j \geq M'_i$ and $P'_i \in b(P'_j, M'_j)$.

To determine an appropriate probability distribution of the marks M'_i , we consider the difference image $B \setminus R$ between the binary image B and the corresponding sphere representation R derived in Section 3, see Figure 13. In particular, we determine all white and black clusters in $B \setminus R$ by means of the Hoshen-Kopelman algorithm, see [39]. For each cluster, both white and black ones, the radius of a sphere with the same volume as the cluster is computed and an exponential distribution with parameter $\vartheta > 0$, shifted by one, is fitted to these radii, i.e., $M'_i - 1 \sim \text{Exp}(\vartheta)$. In our case, we obtain the values $\vartheta = 0.25$, $\vartheta = 0.18$ and $\vartheta = 0.13$ for LSC-750, LSC-850 and LSC-950, respectively.

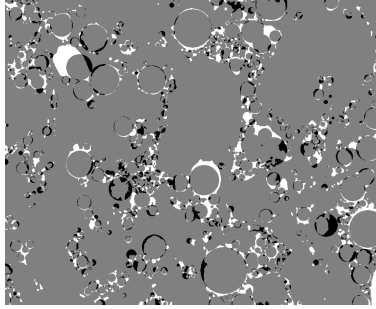


Figure 13: Difference image $B \setminus R$ (with size $7.4 \times 6.0 \mu\text{m}^2$) showing LSC phase detected as pore phase (white) and pore phase detected as LSC phase (black)

Finally, the mark M_i of P_i is defined as follows. In order to assure the connectivity of $\bigcup_{i=1}^{\infty} B_n$, we require that $P\left(\min_{e \in E_{\alpha,c,\delta}^{(n)}(X)} d(b(P_i, M_i), e) > 0\right) = 1$ holds for each $i \geq 1$, where $E_{\alpha,c,\delta}^{(n)}(X)$ denotes the edge set of the random graph $G_{\alpha,c,\delta}^{(n)}(X)$ introduced in Section 4.3. Thus, we put

$$M_i = \begin{cases} \min\left\{M'_i/2, \min_{e \in E_{\alpha,c,\delta}^{(n)}(X)} d(P_i, e)\right\} & \text{if } U_i = 1, \\ -\min\left\{M'_i/2, \max\left\{0, \min_{e \in E_{\alpha,c,\delta}^{(n)}(X)} (d(P_i, e) - 1)\right\}\right\} & \text{otherwise,} \end{cases}$$

where U_1, U_2, \dots are independent and identically distributed random variables with $P(U_i = 0) = P(U_i = 1) = 0.5$.

Note that the spheres $b(P_1, M_1), b(P_2, M_2), \dots$ do not overlap. Furthermore, by the definition of the random radii M_i given above, the connectivity of $\bigcup_{i=n}^{\infty} B_n$ is not destroyed. The intensity of the point process $\{P_i\}$ is chosen such that the specific surface area of $\bigcup_{n=1}^{\infty} B_n$ and B coincide. However, the maximum intensity of a dominance competition model is limited, see [21], and eventually smaller than the required intensity in order to fit the specific surface area of B . In this case we apply the roughening algorithm described above iteratively, until the desired specific surface area of B is reached, see Figure 14. In our case, for the intensity γ the following values are obtained:

$\gamma = 0.01$ for LSC-750, $\gamma = 0.008$ for LSC-850 and $\gamma = 0.0$ for LSC-950.

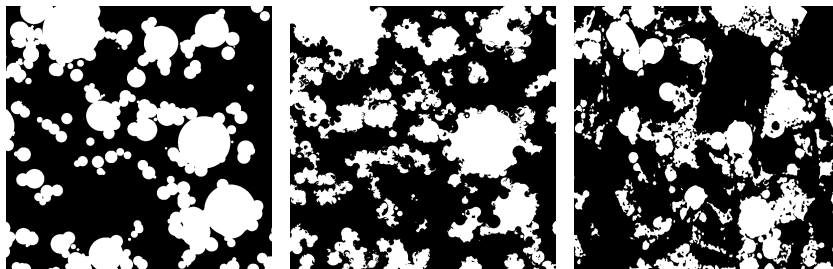


Figure 14: Comparison of simulated 2D-slices before (left) and after (center) surface roughening, together with a 2D slice from real data of LSC-750 (right) on an observation window of size $7.4 \times 6.0 \mu\text{m}^2$

5. Model Validation

Figure 15 shows that there is a good optical resemblance between the binarized LSC images and the corresponding simulated images, which have been drawn from the stochastic microstructure model developed in Section 4.

In addition to this, we can quantitatively evaluate the goodness-of-fit of our stochastic microstructure model, comparing image characteristics which have been computed for the binarized FIB-SEM and simulated data, respectively. In particular, we consider the distribution of spherical contact distances from pore to solid phase, and vice versa, as well as the continuous pore size distribution. Note that these characteristics have not been used for model fitting. Figure 16 shows that these distribution functions computed for simulated data are in a good accordance to those obtained for real data.

Furthermore, for the electrode material considered in the present paper, the geometrical properties of the percolation pathways through the pore and solid phase, respectively, play an important role for the transport of gas-molecules and charges (ions, electrons) within the SOFC electrode. Therefore we investigated the ‘geometric tortuosity’ of the pore space and the LSC phase, which is defined as the relative length of shortest paths along the edges of a certain geometric graph through the pore and LSC phase, respectively, divided by the material thickness. Note that starting from a randomly chosen location on top

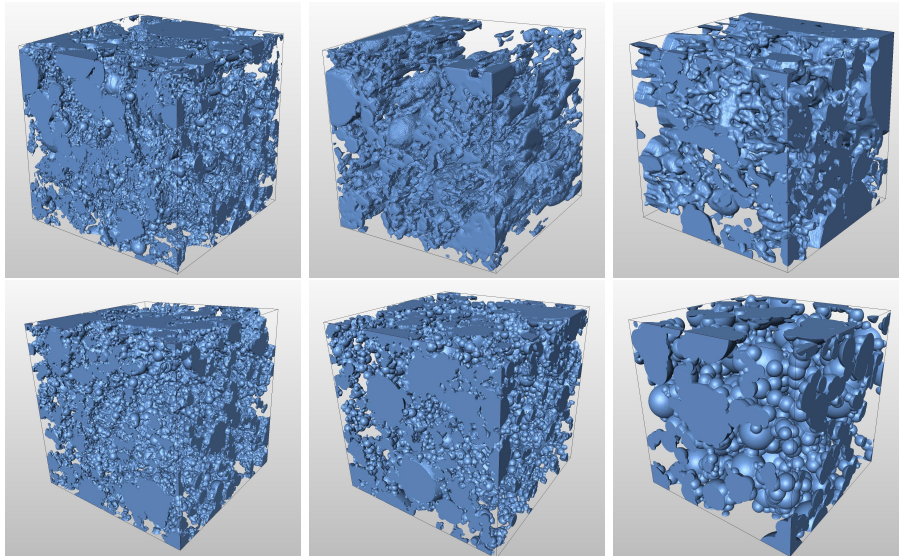


Figure 15: Real data (top) and simulated sphere systems (bottom) for LSC-750 (left), LSC-850 (center) and LSC-950 (right) on a observation window of size $6.0 \times 6.0 \times 6.0 \mu m^3$.

Table 3: Mean geometric tortuosity for pore and LSC phase with respect to voxel size of $7.5 nm^3$

	750°C	850°C	950°C
real data (pore phase)	1.41	1.21	1.41
simulated data (pore phase)	1.46	1.34	1.47
relative error	0.03	0.09	0.04
real data (LSC phase)	1.39	1.26	1.37
simulated data (LSC phase)	1.43	1.40	1.48
relative error	0.02	0.1	0.07

of the porous material, its geometric tortuosity can be represented by a probability distribution instead of looking at the mean tortuosity only, see e.g. [42]. The results given in Table 3 show good coincidence of mean values. This is additionally supported by the small relative error between mean geometric tortuosities of real and simulated data. Although there is no perfect matching, the shapes of the distributions of geometric tortuosity computed for real and simulated data are quite similar, see Figure 17.

6. Conclusions

In the present paper we developed a stochastic model in order to describe and simulate the 3D geometry of two-phase microstructures (solid and pore phase), where the solid phase consists of spherical particles being completely

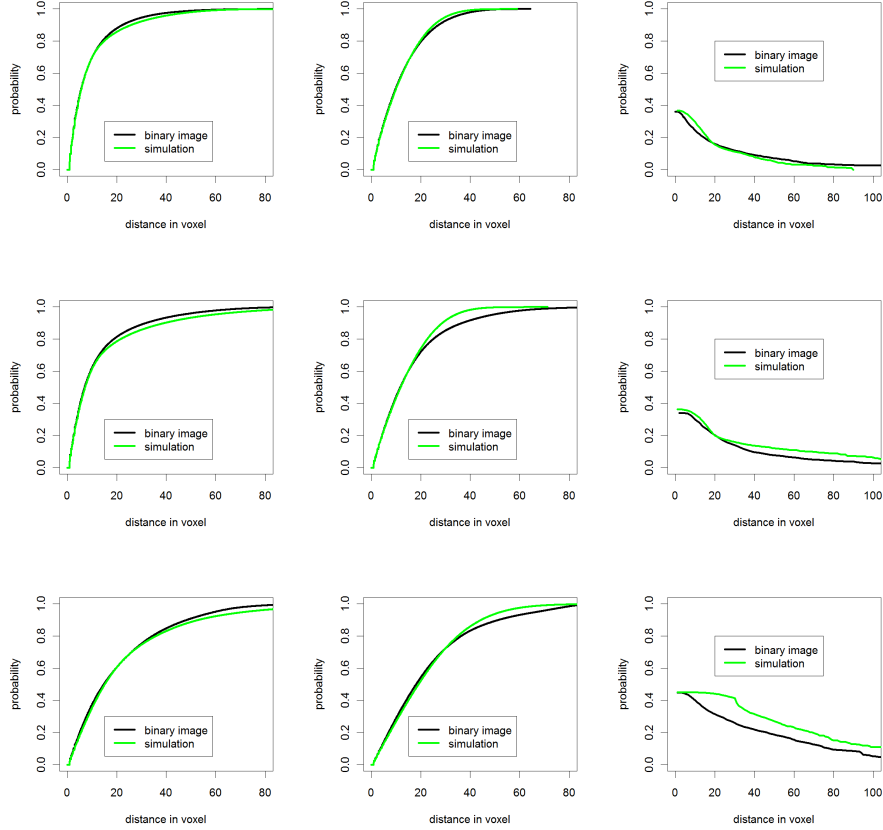


Figure 16: Distribution of contact distances from pore to solid phase (left) and vice versa (center), and continuous pore size distribution (right) for LSC-750 (top row), LSC-850 (center row), and LSC-950 (bottom row)

connected with each other. Such materials appear e.g. in $\text{La}_{0.6}\text{Sr}_{0.4}\text{CoO}_{3-\delta}$ (LSC) cathodes of solid oxide fuel cells, which are produced by screen printing and sintering of a paste consisting of LSC powder manufactured by flame spray synthesis. Thus, as a model type, we considered (fully parameterized) random sphere systems which are based on ideas from stochastic geometry and graph theory. In particular, the midpoints of spheres have been modeled by random point processes. In order to assure the complete connectivity of the spheres, a modified version of the relative neighborhood graph has been introduced. This graph controls the radii of spheres such that a completely connected sphere system is obtained.

Our investigations were based on 3D grayscale images which had been gained by high-resolution FIB-tomography. The parameters of the stochastic microstructure model have exemplarily been fitted to three data sets, representing

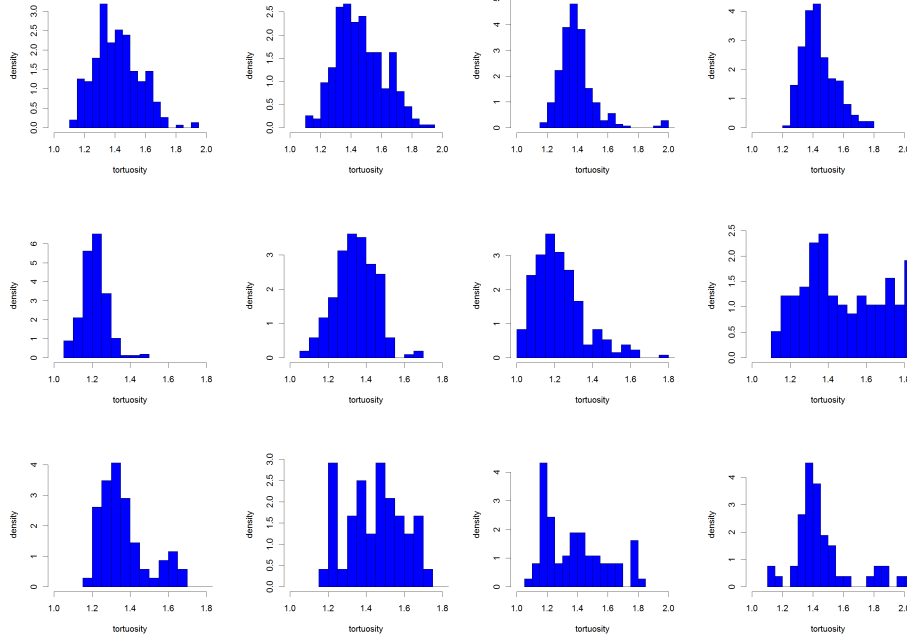


Figure 17: Histograms of geometric tortuosity of pore space (first column: real, second column: simulated) and LSC phase (third column: real, fourth column: simulated) for LSC-750 (top), LSC-850 (center), and LSC-950 (bottom) computed with respect to voxel size 7.5 nm^3

LSC cathodes where the sinter temperature is varied from 750 over 850 to 950°C. The goodness of model-fit has been validated by comparing structural characteristics of real and simulated image data.

The stochastic model can be used to detect quantitative relationships between the production process (e.g. variation of sinter temperatures and/or change of pore former contents) and the resulting microstructures. In a forthcoming paper, the stochastic microstructure model will be combined with physical simulations, e.g. finite element modeling, for virtual scenario analyses. Thereby, model-based morphologies of LSC cathodes will be transformed into grid representations of the microstructures which are used as a basis for FEM, in order to simulate the effect of microstructure variations on the electrode performance (e.g. ohmic resistance, polarization resistance). In this way, the results of our simulations can be used for microstructure optimization while reducing the amount of expensive experiments in real laboratories.

Acknowledgements

The authors would like to thank Andre Heel for providing the LSC nanopowders produced by flame spray synthesis. The software for the analysis of pore

size distributions was provided by Beat Münch which is gratefully acknowledged. FIB-tomography was performed at ETH Zürich with the help of Philippe Gasser. Part of this research has been carried out while Matthias Neumann was visiting the Institute of Computational Physics at Zurich University of Applied Sciences for a period of six months in 2011/12. Last but not least, we are grateful to Christian Hirsch for helpful discussions.

References

- [1] L. Holzer, B. Iwanschitz, T. Hocker, B. Münch, M. Prestat, D. Wiedenmann, U. Vogt, P. Holtappels, J. Sfeir, A. Mai and T. Graulen (2011). Microstructure degradation of cermet anodes for solid oxide fuel cells: Quantification of nickel grain growth in dry and in humid atmospheres. *Journal of Power Sources*, **196**, 1279-1294.
- [2] L. Holzer, B. Münch, B. Iwanschitz, M. Cantoni, T. Hocker and T. Graule (2011). Quantitative relationships between composition, particle size, triple phase boundary length and surface area in nickel-cermet anodes for Solid Oxide Fuel Cells. *Journal of Power Sources*, **196**, 7076-7089.
- [3] A. Iwanschitz, J. Sfeir, A. Mai and M. Schütze (2010). Degradation of SOFC anodes upon redox cycling: A comparison between Ni/YSZ and Ni/CGO. *Journal of the Electrochemical Society*, **157**(2), 269-278.
- [4] P. R. Shearing, J. Golbert, R. J. Chater and N. P. Brandon (2009). 3D reconstruction of SOFC anodes using a focused ion beam lift-out technique. *Chemical Engineering Science*, **64**, 3928-3933.
- [5] N. Shikazono, D. Kanno, K. Matsuzaki, H. Teshima, S. Sumino and N. Kasagi (2010). Numerical Assessment of SOFC anode polarization based on three-dimensional model microstructure reconstructed from FIB-SEM images. *Journal of the Electrochemical Society*, **157**, B665-B672.
- [6] J. R. Wilson, W. Kobsiriphat, R. Mendoza, H. Y. Chen, J. M. Hiller, D. J. Miller, K. Thornton, P.W. Voorhees, S. B. Adler and S. A. Barnett (2006). Three-dimensional reconstruction of a solid-oxide fuel-cell anode. *Nature Materials*, **5**, 542-544.
- [7] M. Prestat, J.F. Koenig and L.J. Gauckler (2007). Oxygen reduction at thin dense $La_{0.52}Sr_{0.48}Co_{0.18}Fe_{0.82}O_{3-\delta}$ electrodes. Part I: reaction model and faradaic impedance. *Journal of Electroceramics*, **18**, 87.
- [8] J. Mantzaras, S.A. Freunberger, F.N. Büchi, M. Roos, W. Brandstätter, M. Prestat, L.J. Gauckler, B. Andreaus, F. Hajbolouri, S.M. Senn, D. Poulidakos, A.K. Chaniotis, D. Larrain, N. Autissier and F. Maréchal (2004). Fuel cell modelling and simulations. *International Journal for Chemistry*, **58**, 857.

- [9] A. Evans, S. Karalić, J. Martynczuk, M. Prestat, R. Tölke and L.J. Gauckler (2012). $La_{0.6}Sr_{0.4}CoO_{3-\delta}$ thin films prepared by pulsed laser deposition as cathodes for micro-solid oxide fuel cells. *ECS Transactions*, **45(1)**, 333.
- [10] J. Hayd, L. Dieterle, U. Gruntow, D. Gerthsen and E. Ivers-Tiffée (2011). Nanoscaled $La_{0.6}Sr_{0.4}CoO_{3-\delta}$ as intermediate temperature solid oxide fuel cell cathode: Microstructure and electrochemical performance. *Journal of Power Sources*, **196**, 7263-7270.
- [11] H.S. Noh, H. Lee, H.I. Ji, H.W. Lee, J.H. Lee and J.W. Son (2011). Limitation of Thickness Increment of Lanthanum Strontium Cobaltite Cathode Fabricated by Pulsed Laser Deposition. *Journal of the Electrochemical Society*, **158**, B1-B4.
- [12] M. Prestat, A. Infortuna, S. Korrodi, S. Rey-Mermet, P. Murralt and L. J. Gauckler (2007). Oxygen reduction at thin dense $La_{0.52}Sr_{0.48}Co_{0.18}Fe_{0.82}O_{3-\delta}$ electrodes. *Journal of Electroceramics*, **18**, 111-120.
- [13] M. Prestat, A. Morandi, A. Heel, L. Holzer, P. Holtapperls and T. J. Graule (2010). Effect of graphite pore former on oxygen electrodes prepared with $La_{0.6}Sr_{0.4}CoO_{3-\delta}$ nanoparticles. *Electrochemistry Communications*, **12**, 292-295.
- [14] S. B. Adler, J. A. Lane and B. C. H. Steele (1997). Fundamental issues in modeling of mixed-conductors. Rebuttal to "Comment on 'Electrode kinetics of porous mixed-conducting oxygen electrodes'". *Journal of the Electrochemical Society*, **143**, 3554-3556.
- [15] D. Beckel, U. P. Muecke, T. Gyger, G. Florey, A. Infortuna and L. J. Gauckler (2007). Electrochemical performance of LSCF based thin film cathodes prepared by spray pyrolysis. *Solid State Ionics*, **178**, 407-415.
- [16] G. W. Coffey, L. R. Perderson and P. C. Rieke (2003). Competition between bulk and surface pathways in mixed ionic electronic conducting oxygen electrodes. *Journal of the Electrochemical Society*, **150**, 39-51.
- [17] Y. Lu, C. Kreller and S.B. Adler (2009). Measurement and Modeling of the Impedance Characteristics of Porous $La_{1-x}Sr_xCoO_{3-\delta}$ Electrodes. *Journal of the Electrochemical Society*, **156(4)**, B513-B525.
- [18] S. B. Adler (2004). Factors governing oxygen reduction in solid oxide fuel cell cathodes. *Chemical Reviews*, **104**, 4791-4844.
- [19] L. Holzer and M. Cantoni (2012). Review of FIB-Tomography. In: Nanofabrication using Focused Ion and Electron Beams: Principles and Applications. Eds. I. Utke, S.A. Moshkalev New York: Oxford University Press.

- [20] R. Thiedmann, A. Spettl, O. Stenzel, T. Zeibig, J. C. Hindson, Z. Saghi, N. C. Greenham, P. A. Midgley and V. Schmidt (2012). Networks of nanoparticles in organic-inorganic composites: Algorithmic extraction and statistical analysis. *Image Analysis and Stereology*, **31**, 23-42.
- [21] J. Illian, A. Penttinen, H. Stoyan and D. Stoyan (2008). Statistical Analysis and Modelling of Spatial Point Patterns. Chichester: J. Wiley & Sons.
- [22] D. Stoyan, W. S. Kendall and J. Mecke (1995). Stochastic Geometry and its Applications. 2nd ed., Chichester: J. Wiley & Sons.
- [23] O. Stenzel, H. Hassfeld, R. Thiedmann, L. J. A. Koster, S. D. Oosterhout, S. S. van Bavel, M. M. Wienk, J. Loos, R. A. J. Janssen and V. Schmidt (2011). Spatial modeling of the 3D morphology of hybrid Polymer-ZnO solar cells, based on electron tomography data. *Annals of Applied Statistics*, **5**, 1920-1947.
- [24] R. Thiedmann, O. Stenzel, A. Spettl, P. R. Shearing, S. J. Harris, N. P. Brandon and V. Schmidt (2011). Stochastic simulation model for the 3D morphology of composite materials in Li-ion batteries. *Computational Materials Science*, **50**, 3365-3376.
- [25] C. Hirsch, D. Neuhäuser and V. Schmidt (2012). Connectivity of random geometric graphs related to minimal spanning forests. *Advances in Applied Probability* (submitted).
- [26] A. Heel, P. Holtappels and T. Graule (2010). On the synthesis and performance of flame-made nanoscale $\text{La}_{0.6}\text{Sr}_{0.4}\text{CoO}_{3-\delta}$ and its influence on the application as an intermediate temperature SOFC cathode. *Journal of Electroceramics*, **195**, 6709-6718.
- [27] L. Holzer, F. Indutnyi, P. Gasser, B. Münch and M. Wegmann (2004). 3D analysis of porous BaTiO₃ ceramics using FIB nanotomography. *Journal of Microscopy*, **216**(1), 84-95.
- [28] L. Holzer and B. Münch (2009). Towards reproducible three-dimensional microstructure analysis of granular materials and complex suspensions. *Microscopy and Microanalysis*, **15**, 130-146.
- [29] M. D. Uchic, L. Holzer, B. J. Inkson, E. L. Principe and P. Munroe (2007). 3D microstructural characterization using focused ion beam tomography. *MRS Bulletin*, **32**, 408-416.
- [30] Avizo 7 - 3D analysis software for scientific and industrial data. <http://www.vsg3d.com/avizo/overview>. 2012.
- [31] Fiji - open source software. <http://fiji.sc/wiki/index.php/Fiji/>. 2011.
- [32] B. Münch and L. Holzer (2008). Contradicting geometrical concepts in pore size analysis with electron microscopy and mercury intrusion. *Journal of the American Ceramic Society*, **91**, 4053-4067.

- [33] M. Seul, L. O’Gorman and M. J. Sammon (2008). Practical Algorithms for Image Analysis. Cambridge: Cambridge University Press.
- [34] R. Beare and G. Lehmann (2006). The watershed transform in ITK - discussion and new developments. *The Insight Journal*, Id: 92.
- [35] S. Beucher and F. Meyer (1989). The morphological approach to segmentation: The watershed transformation. *Mathematical Morphology in Image Processing, Optical Engineering*, **34**, 433-481.
- [36] J.B.T.M Roerdink and A. Meijster (2000). The watershed transform: Definition, algorithms and parallelization strategies. *Fundamenta Informaticae*, **41**, 187-228.
- [37] W. Burger and M. J. Burge (2007). Digital Image Processing - An Algorithmic Approach using Java. Berlin: Springer.
- [38] B. Jähne (2005). Digital Image Processing. 6th ed., Berlin: Springer.
- [39] J. Hoshen and R. Kopelman (1976). Percolation and cluster distribution. I. Cluster multiple labeling technique and critical concentration algorithm. *Physical Review B*, **14**, 3438-3445.
- [40] G. T. Toussaint (1980). The relative neighbourhood graph of a finite planar set. *Pattern Recognition*, **12**, 261-268.
- [41] T. Saito and J. I. Toriwaki (1994). New algorithms for euclidean distance transformation of an n -dimensional digitized picture with applications. *Pattern Recognition*, **27**, 1551-1565.
- [42] R. Thiedmann, C. Hartnig, I. Manke, V. Schmidt and W. Lehnert (2009). Local structural characteristics of pore space in GDL’s of PEM fuel cells based on geometric 3D graphs. *Journal of the Electrochemical Society*, **156**, B1339-B1347.